ACS APPLIED MATERIALS & INTERFACES

Research Article

Cite This: ACS Appl. Mater. Interfaces 2019, 11, 26559−26570

www.acsami.org

Understanding the Stiff-to-Compliant Transition of the Meniscal Attachments by Spatial Correlation of Composition, Structure, and Mechanics

Alexander J. Boys,[†] Jennie A. M. R. Kunitake,[†] Corinne R. Henak,[‡] Itai Cohen,[§] Lara A. Estroff,[†,∥] and Lawrence J. Bonassar*[,‡,⊥]

[†]Department of Materials Science & Engineering, [‡]Meinig School of Biomedical Engineering, [§]Department of Physics, [∥]Kavli Institute at Cornell for Nanoscale Science, and [⊥]Sibley School of Mechanical Engineering, Cornell University, Ithaca, New York 14853, United States

Supporting Information

ABSTRACT: Recently, the scientific community has shown considerable interest in engineering tissues with organized compositional and structural gradients to mimic hard-to-soft tissue interfaces. This effort is hindered by an incomplete understanding of the construction of native tissue interfaces. In this work, we combined Raman microscopy and confocal elastography to map compositional, structural, and mechanical features across the stiff-to-compliant interface of the attachments of the meniscus in the knee. This study provides new insight into the methods by which biology mediates multiple orders of magnitude changes in stiffness over tens of microns. We identified how the nano- to mesoscale architecture mediates complex microscale transitional regions across the interface: two regions defined by chemical composition, five distinguished by structural features, and three mechanically distinct regions. We identified three major components that lead to a robust interface between a soft tissue and bone: mobile collagen fiber units, a continuous interfacial region, and a local stiffness gradient. This tissue architecture allows for large displacements of collagen fibers in the attachments, enabling meniscal movement without localizing strains to the soft tissue-to-bone interface. The interplay of these regions reveals a method relying on hierarchical structuring across multiple length scales to minimize stress concentrators between highly dissimilar materials. These insights inspire new design strategies for synthetic soft tissue-to-bone attachments and biomimetic material interfaces.

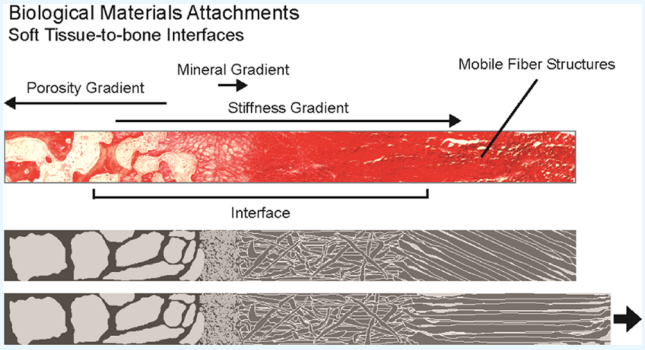

KEYWORDS: *enthesis, soft tissue-to-bone interface, tissue gradients, mechanical properties, Raman spectroscopy, elastography, mapping*

INTRODUCTION

A host of recent studies have focused on the challenges of engineering interfaces that integrate stiff and compliant materials for biological applications.[1−11] In contrast to typical material interfaces, biological interfaces can mediate multiple orders of magnitude changes in stiffness over tens of microns.[14−20] A subset of these interfacial tissue systems, called entheses, are found at the ends of ligaments, tendons, and the meniscus. Entheses anchor these structures to bone, making them essential musculoskeletal junctions that provide motion and stability in the body. Specifically, the meniscus acts as a shock absorber, redistributing high axial loads that develop in the knee into radial strains within the meniscal tissue.[21] It is able to perform this function through its entheses, which bind the meniscus to the bone. The large change in stiffness between these materials, ∼100 kPa in the meniscus to ∼20 GPa in the bone, is manifested in similarly steep changes in local tissue strains.[22,23] Typical engineered material interfaces, as well as some biological materials, utilize gradual changes in stiffness, on the order of millimeters, to minimize stress concentrations.[12,13] Entheses lack these long-range stiffness gradients, indicating that stress mitigation must occur through a different mechanism.[20] Elucidating these mechanisms requires high-resolution imaging of structure and composition coupled with spatially resolved maps of the mechanics at a similar resolution. Here, we integrate data from Raman microscopy and confocal elastography to provide a multimodal picture of the microscale function of the meniscal enthesis.

Biological characterization of entheses using histological analysis has revealed four distinct regions: bone, calcified fibrocartilage, uncalcified fibrocartilage, and ligamentous tissue.[24,25] These regions vary in composition, structure, and

Received: February 26, 2019
Accepted: July 3, 2019
Published: July 3, 2019

DOI: 10.1021/acsami.9b03595
ACS Appl. Mater. Interfaces 2019, 11, 26559−26570

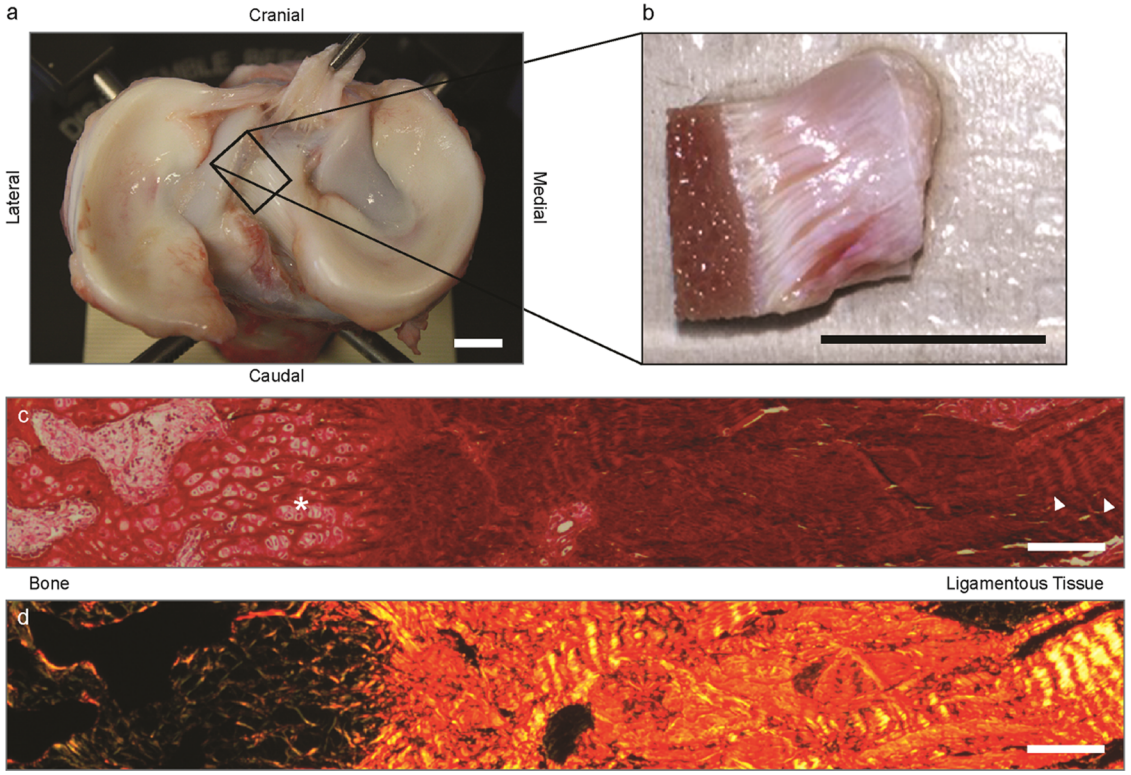

Figure 1. Anatomy and structure of the meniscal enthesis. (a) Tibial plateau of a neonatal bovid. The menisci, semilunar, fibrocartilaginous discs, situated on the lateral and medial sides of the knee joint, are anchored into the bone through their entheses. The boxed area is the approximate location for the meniscal enthesis explant. Medial caudal entheses were used for analysis. This enthesis inserts into the tibial plateau along a sloping interface. The angle of this sloping interface varies, so transverse planes were analyzed as pictured in remaining figures. (b) Meniscal enthesis, flattened using a cryotome, thereby generating samples for Raman microscopy and confocal elastography that were square millimeters in cross-sectional area dependent on anatomy. The bone is on the left of the sample and the soft tissue is on the right. (c) Picrosirius Red stain for collagen of demineralized enthesis under white light. The sample shows the trabecular structure on the left moving through an intermediate fibrocartilaginous region to a denser collagen region to large collagen fibers on the far right. The star indicates the fibrocartilaginous morphology, and arrows point to collagen fibers. (d) Picrosirius Red stain of the same area of the enthesis as (c) under cross-polarized light. Color and color intensity are correlated with collagen fiber diameter and degree of orientation.[76,77] Collagen becomes oriented after crossing through the intermediate fibrocartilage. Large, crimped fibers are visible on the far right of the image, consistent with the collagen fibers in (c). Scale bars for (a) and (b) are 1 cm. Scale bars for (c) and (d) are 200 μm.

mechanics,[14−19,26] but the link between the composition and structure of the tissue and the mechanical behavior of the enthesis is not fully understood.[16,18,20,27,28] In addition, the previous literature has shown the presence of different compositional features in other entheses that are not visible through histology, such as a gradient in the mineral content at the interface between mineralized and unmineralized tissues.[26,29,30] Structural features have also been noted, such as the gradients in the degree of misalignment in collagen orientation across the interface and the presence of a splayed fibrillar region in the fibrocartilage of the enthesis, where fibers (∼10s of microns) transition to fibrils (∼10−100s of nanometers).[16,18,31,32] Current theories suggest that movement of individual fibers and fibrils, relating to the different orientations of collagen across these regions, plays a prevalent role in enthesis function.[33] These examples indicate that enthesis composition and structure are more intricate than can be understood through histological analysis and raise the question of the role of composition and structure in the mechanical behavior of the enthesis. Elucidating the mechanism(s) that enables this rapid change in stiffness requires an analysis that can spatially correlate composition, structure, and function at a scale that is relevant to the tissue.

Applying material characterization techniques to these interfaces enables spatial correlation of compositional and mechanical data at the microscale.[34−39] For example, Raman microscopy provides a means for producing compositional and structural images with micrometer resolution. This technique relies on detecting molecular vibrations to map the distribution of unique chemical species within the sample and is capable of detecting multiple chemical species that are intermixed at the nanoscale.[40] This type of analysis is particularly important for hierarchically structured tissues, such as bone and entheses, as these types of tissue rely on intimate intermixing of dissimilar materials (e.g., apatite crystals and collagen fibrils) at the nanoscale to function mechanically.[22] Further, this technique does not require fixation or dehydration of the tissue, allowing for direct comparison to mechanical data.[36,41−45] Confocal elastography, which uses imaging of applied deformations on a material to calculate spatially resolved strains, can probe mechanical behavior of the tissue at the same microscale resolution as Raman microscopy.[46−51] Although Raman microscopy and confocal elastography have each been used separately to interrogate the hard and soft tissue components of entheses,[17,18,51] they have not been used in combination to probe across the interface. Here, we combine these techniques to examine the compositional, structural, and mechanical

DOI: 10.1021/acsami.9b03595
ACS Appl. Mater. Interfaces 2019, 11, 26559−26570

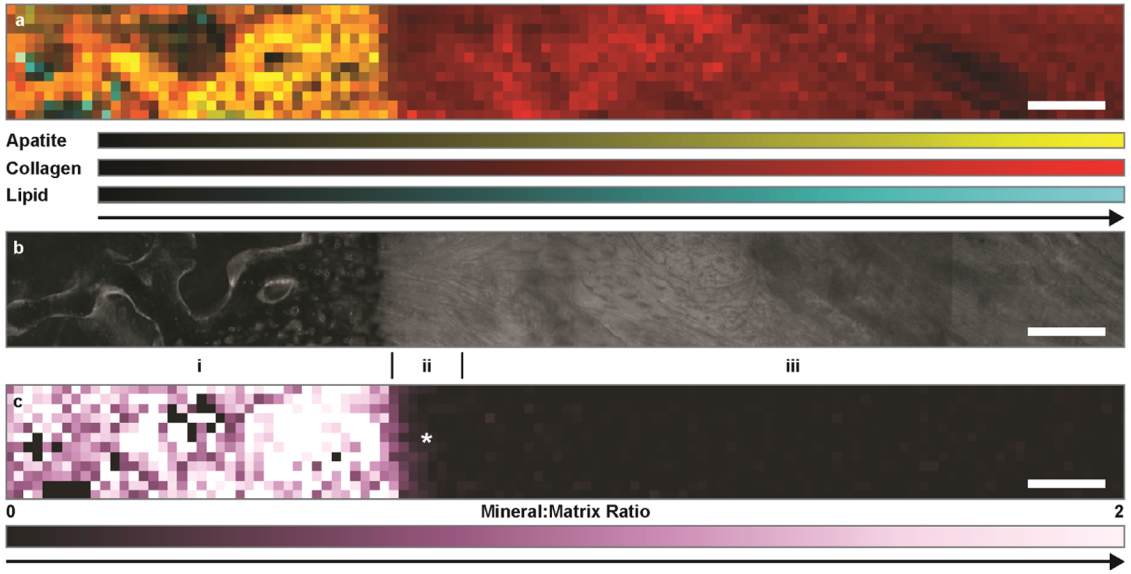

Figure 2. Morphological and compositional analyses using Raman microscopy. (a) Representative composite Raman peak area maps of apatite (950−980 cm^{-1}), collagen (833−905, 1224−1296, 1439−1484, 2908−3028 cm^{-1}), and lipid (1278−1326, 1423−1468, 2835−2870 cm^{-1}).[72,73] A typical trabecular structure can be seen on the left side of the image transitioning to the oriented collagen on the right side of the image. The intermediate region contains a tissue similar in appearance to the calcified fibrocartilage before crossing into the soft tissue region. (b) Confocal fluorescence image of the same region as (a). Fluorescence is derived from 5-(4,6-dichlorotriazinyl) aminofluorescein (5-DTAF), a general protein stain. The image is constructed from multiple stitched images. (c) The mineral:matrix image of the same region of enthesis as (a) and (b). The mineral/matrix (950−980/1224−1296 cm^{-1}) peak area ratio map is plotted for values from 0 to 2. Compositional regions are demarcated: mineralized tissue (M) and unmineralized tissue (UM) with a gradient visible between the regions. Scale bars for all images are 200 μm. The asterix indicates the location of the gradient. See Supporting Information, Figures S3 and S4 for n = 2−6.

properties of meniscal entheses and develop a framework for understanding the structure−function relationship in this tissue at the microscale.

RESULTS AND DISCUSSION

Enthesis Morphology Transitions from Porous Trabecular Bone into Large, Oriented Collagen Fibers. At the macroscale, the fibrocartilaginous meniscus transitions to microscale, preferentially oriented collagen fibers that insert into the tibial plateau over a sloping, subsurface interface (Figure 1a and the Supporting Information, Figure S1). We explanted this area from neonatal bovids for further analysis of this tibial insertion (Figure 1b). A morphological analysis of the enthesis through Picrosirius Red staining for collagen shows a transition from bony trabeculae to large, oriented collagen fibers, where orientation is evident by color changes in the polarized light image (Figure 1c,d). The intermediate area between the trabecular bone and the oriented fibers contains various interfacial regions, visible by changes in the morphology. The trabecular pores of the bone appear to show smaller diameters before transitioning to the fibrocartilaginous tissue. The intermediate area between the trabecular bone of the tibial plateau and the oriented fibers in the bulk of the enthesis displays a fibrocartilaginous region followed by microscale transitions in morphology and collagen orientation (Figure 1c,d).

To measure changes in the composition and structure that occur across this area, Raman microscopy was used to map large areas (~500 μm × 4000 μm) from the bone to ligamentous material (Figure 2). Explanted entheses were flattened using a cryotome to facilitate optical analysis through Raman microscopy (n = 6). These samples were placed in phosphate-buffered saline (PBS) to maintain hydration for all experiments performed in this study. Spectral analysis shows a shift from the bony tissue (mineralized collagen), indicated by the presence of the phosphate and carbonate peaks of the carbonate-substituted apatite coupled with amide and CH peaks consistent with collagen signatures, to soft collagenous tissue, where the proline/hydroxyproline peaks of collagen are no longer obscured by apatite peaks. The presence of a lipidous material was also detected (Supporting Information, Figure S2). Composite Raman images (Figure 2a) show a transition from the mineralized tissue to oriented collagenous material. The mineralized tissue has a typical trabecular structure. The lipidous material is present in the pores of the trabeculae, likely representing the bone marrow.[44] An intermediate region that appears similar in morphology to the calcified fibrocartilage is observed near the interface. Although the morphology of the enthesis exhibits some sample-to-sample variations, the overall structure remains the same, showing a shift from the trabecular bone through intermediate interfacial regions to the oriented soft tissue (the Supporting Information, Figure S3). Structural features in this Raman composite image correlate with a confocal fluorescence image of the same region (Figure 2b), providing spatially resolved morphological and compositional measurements.

Transition from Mineralized to Unmineralized Tissue Occurs through a Gradient. To quantitatively define the compositional changes across the enthesis, mineral/matrix peak area ratio maps were constructed from Raman data (Figure 2c and Supporting Information, Figure S4).[52,53] The images reveal a shift from the mineralized (M) to unmineralized (UM)[a] tissue through an intermediate gradient region, similar to that observed in other entheses.[17,26,30,31] The intermediate gradient region has a length of 188 ± 56 μm (n = 6), where the tissue transitions from the mineralized to

DOI: 10.1021/acsami.9b03595
ACS Appl. Mater. Interfaces 2019, 11, 26559−26570

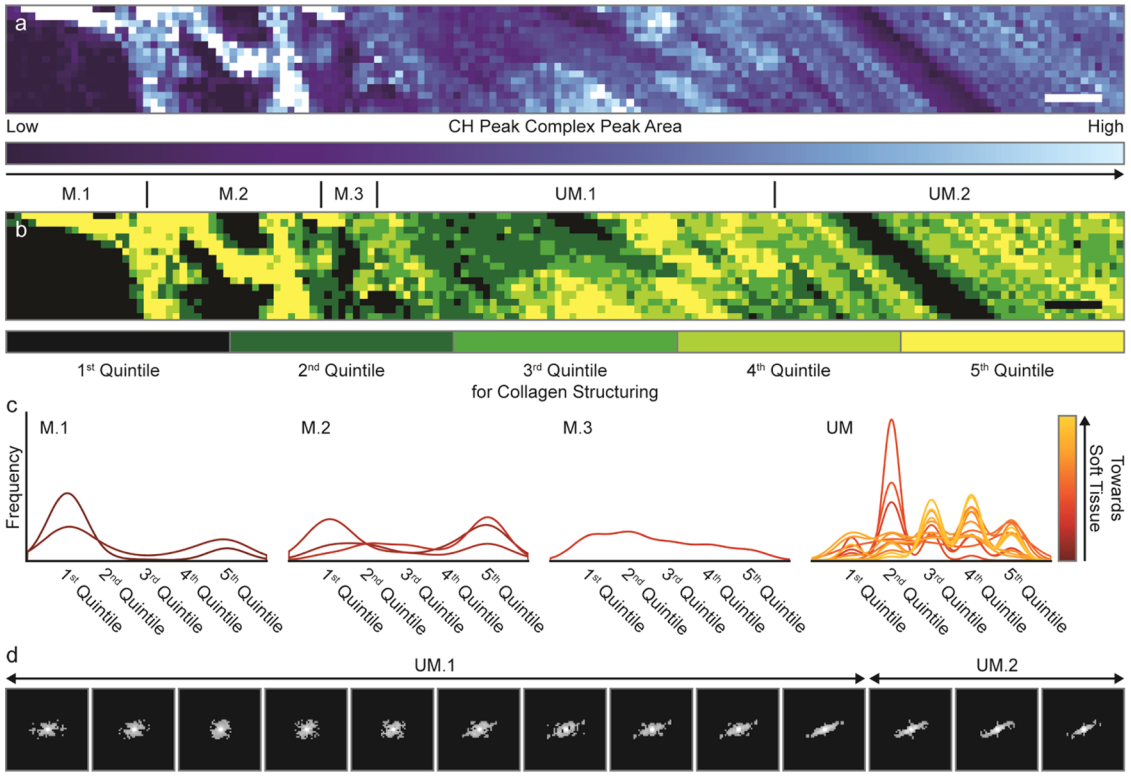

Figure 3. Structural analysis using Raman microscopy. (a) Representative Raman image of the collagen-specific portion of the CH peak complex (2908−3028 cm^{-1}) area. The color bar is scaled from 0 to 50 000. A trabecular structure is visible on the left of the image and oriented fibers are visible on the right. We used collagen-specific portions of the CH peak complex to map collagen content, because these are generally the largest spectral signatures in the tissue and are sensitive to fine changes in topology and morphology. (b) Quintile-plotted image of the same area for collagen structuring. Structural regions are demarcated: open trabeculae (M.1), dense trabeculae (M.2) (567 ± 266 μm), transitional region (M.3) (200 ± 126 μm), disorganized bundles (UM.1) (1008 ± 367 μm), oriented fibers (UM.2). (c) Textural histogram-based analysis of collagen structuring data. For presentation, histograms are shown as continuous lines rather than bars. Histograms are plotted per region: open trabeculae (M.1), dense trabeculae (M.2), transitional region (M.3), remaining tissue, which was found to correspond with the unmineralized tissue (UM). (d) Fast Fourier transform (FFT)-based analysis of orientation for the remaining tissue. FFTs are collected on a per-pixel sliding window, one third the size of the remaining tissue, starting at the end of the transitional region (M.3). Every sixth FFT, including first and last, is plotted to show changes in orientation between disorganized bundles (UM.1) and oriented fibers (UM.2). The demarcation for the last two regions is shown above FFTs and is determined through the calculated orientation index. Scale bars for all images are 200 μm. See Supporting Information, Figures S5 and S6 for n = 2−6.

unmineralized collagenous tissue. The length of this gradient is similar to the size of mineral gradients observed in ligament and tendon entheses[17,26,31] but could appear elongated in this analysis by subsurface sloping of the interface in the meniscal enthesis (Supporting Information, Figure S1). In addition to the gradient region, a band where the mineral/matrix ratio is higher than the surrounding tissue is empirically visualized immediately prior to the gradient region, but the analysis of secondary apatite-related peaks would be required to test the validity of the presence of this band (Supporting Information, Figure S4). Overall, spatial analysis of mineral/matrix ratio images divides the enthesis into two compositionally distinct regions connected through a gradient.

Compositional Regions of the Enthesis can be Further Sub-divided into Structurally Distinct Regions. To further understand the structure−function relationship of the enthesis, we developed a method for quantifying details of the microscale collagen architecture. Our analysis indicates the presence of five major structural regions: open trabeculae (M.1), dense trabeculae (M.2), a transitional region (M.3), disorganized bundles (UM.1), and oriented fibers (UM.2) (Figure 3). To identify the locations and transitions between these different regions and their relation to the composition, we used Raman images derived from spectral signatures and registered them with our compositional data. In particular, we used maps of the collagen-related portions of the CH peak complex, as it shows little polarization dependence and is sensitive to fine changes in the tissue morphology and topology due to its high peak intensity (Figure 3a and Supporting Information, Figure S2). To normalize these data between multiple samples, we divided the distribution of the peak areas of the CH peak complex for each sample into five even quintiles and replotted these maps according to quintile distributions (Figure 3b). Dividing the data into quintiles both normalizes the images between samples and segments certain structural features. For example, pores were empirically found to fall within the first quintile. Using data from these normalized images, a textural analysis was performed to quantify the collagen architecture. The textural analysis spatially binned each sample into 200 μm wide regions and examined histograms of the distribution of pixels within those bins. Using this method (Supporting Information, Figures S5−S7), we identified fingerprints of structural regions based on histogram shapes that were consistently identified across multiple samples: open trabeculae (M.1), dense trabeculae (M.2), a transitional region (M.3), and the remaining tissue,

DOI: 10.1021/acsami.9b03595
ACS Appl. Mater. Interfaces 2019, 11, 26559−26570

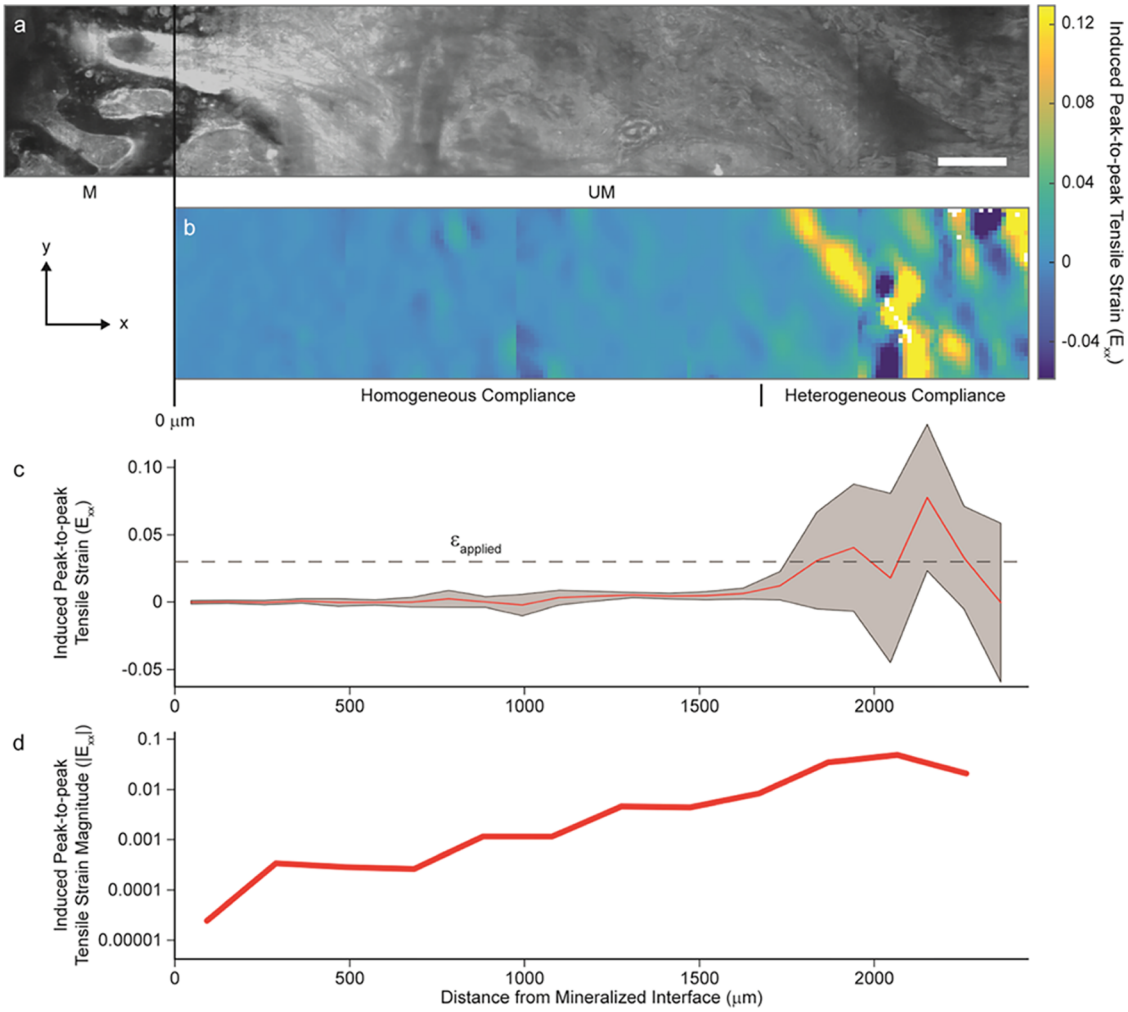

Figure 4. Mechanical analysis using confocal fluorescence elastography. (a) Representative confocal fluorescence image of the enthesis sample. (b) Peak-to-peak E_{xx} Langrangian finite strain map at frame 10 (peak in loading cycle) starting at the mineralized interface with the coordinate system corresponding to the confocal fluorescence image from (a). Mineralized tissue (M) and unmineralized tissue (UM) are identified. Additionally, within the unmineralized tissue (UM), the homogeneous compliant region (1310 ± 506 μm) and the heterogeneous compliant regions are identified. (c) Average peak-to-peak E_{xx} Langrangian finite strain as a function of distance from the mineralized interface at frame 10. The red line is the average strain, and the gray region shows the standard deviation. Average strains are binned at 100 μm for clarity. (d) Average peak-to-peak E_{xx} Langrangian finite strain magnitude on a semilog plot as a function of distance at frame 10. Strains are binned at 200 μm for clarity. (c) and (d) are scaled to match the images in (a) and (b). Scale bar is 200 μm. See Supporting Information, Figures S9 and S10 for n = 2−6.

which was identified to be spatially consistent with the location of the unmineralized tissue region (UM) (Figure 3b,c).

Open trabeculae (M.1) were distinguishable through high frequencies in the first quintile with lower frequencies in the fifth quintile, indicating large porous areas, as the first quintile corresponds to little or no Raman signal. Dense trabeculae (M.2) were distinguishable by low frequencies in the first quintile with high frequencies in the fifth quintile, showing a structure with lower porosity. The tissue structure shifts through a transitional region (M.3) between the trabeculae and the remaining tissue, distinguishable through a broad, flat histogram. Given that these maps are derived from the same spectral data as the compositional analysis, we can spatially register mineralized regions, noting that the trabecular regions and the transitional region are all mineralized, indicating nanoscale apatitic mineral embedded in a collagen matrix. The transitional region demarcates the trabecular structure from the remaining tissue. Thus, our textural analysis reveals that the compositionally derived mineralized region can be broken up into open trabeculae (M.1), dense trabeculae (M.2), and a transitional region (M.3).

The unmineralized region does not show distinctive trends through textural analysis, but a visual analysis implies a change in overall collagen orientation. To quantify this change, within the unmineralized region, two-dimensional (2D) fast Fourier transforms (FFTs) of a sliding window within the normalized Raman images (Figure 3b) were collected and filtered for analysis (Supporting Information, Figures S6, S8, and Movies 1−6). The onset of the oriented tissue was defined through an index related to the orientation of a sliding window FFT. This FFT analysis shows that the unmineralized tissue can be divided into two regions: disorganized bundles (UM.1) and oriented fibers (UM.2) (Figure 3d).

By combining these two approaches (textural and FFT analyses), five structural regions were identified for n = 6 samples: open trabeculae (M.1), dense trabeculae (M.2) (567 ± 266 μm), a transitional region (M.3) (200 ± 126 μm),

DOI: 10.1021/acsami.9b03595
ACS Appl. Mater. Interfaces 2019, 11, 26559−26570

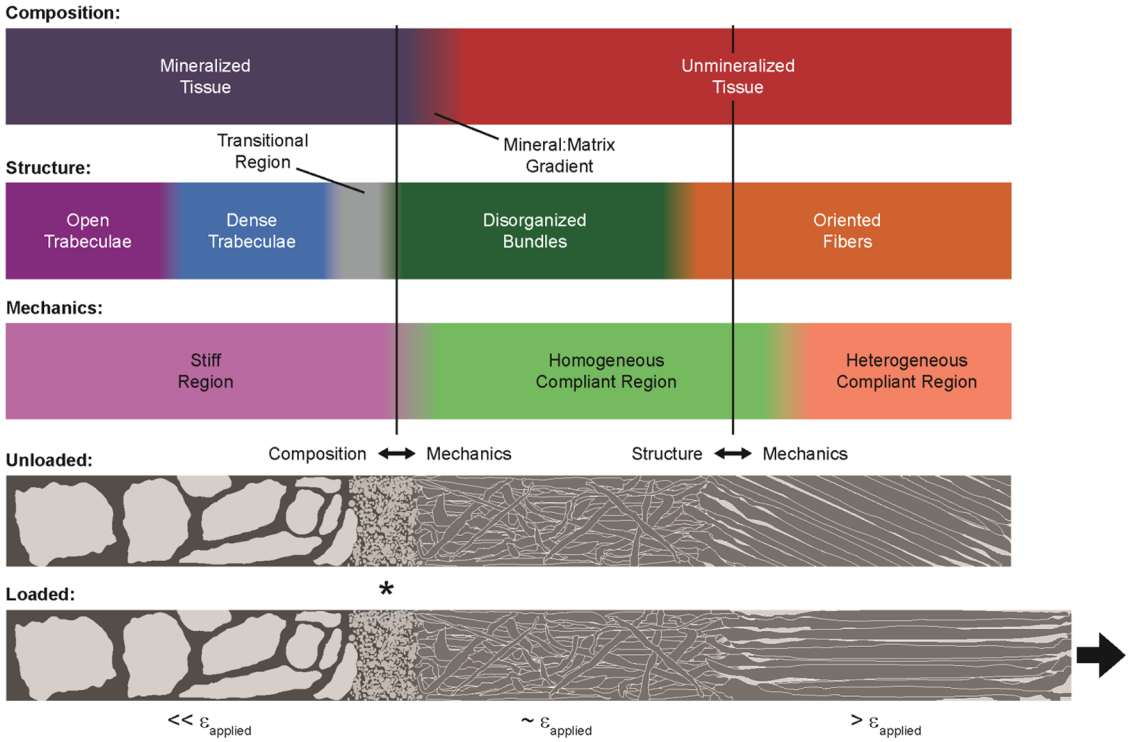

Figure 5. Schematic view of the regional changes in the enthesis followed by the resulting mechanics. Regions are plotted to accurately reflect the size and position of regions with respect to one another. Two compositional regions were found: mineralized (M) and unmineralized (UM) tissues, which are separated by a mineral/matrix gradient (188 ± 56 μm). Five structural regions were found: open trabeculae (M.1), dense trabeculae (M.2) (567 ± 266 μm), transitional region (M.3) (200 ± 126 μm), disorganized bundles (UM.1) (1008 ± 367 μm), and oriented fibers (UM.2). Three mechanical regions were found: a stiff region, a homogeneous compliant region (1310 ± 506 μm), and a heterogeneous compliant region. The first mechanical transition is dictated by the composition, whereas the second is dictated by the structure, as indicated. A corresponding schematic of an enthesis is shown on the bottom in unloaded and loaded configurations. High structural strains develop in the region of oriented fibers on the right during loading. Strains are reduced into the mineralized tissue, which gradually transitions into the porous tissue that extends through the remainder of the bone in the proximal tibia. The fibrocartilaginous region is indicated by the star in the schematic.

disorganized bundles (UM.1) (1008 ± 367 μm), and oriented fibers (UM.2).

Confocal Elastography Reveals Strain Gradients across the Enthesis. The mechanical behavior of the enthesis was analyzed to understand how the enthesis performs under physiologic loading conditions. To perform this analysis on the tissue, deformations were applied with a piezoelectrically actuated load frame and imaged on a confocal microscope.[48−51] For analysis, flattened, hydrated samples (n = 6) were prestressed and submerged in PBS, a fluid that possesses a similar ionic strength and osmolarity to biological fluids, in a hydration plate. The hydration plate was mounted into a load frame that sits on the top of an inverted confocal microscope.[48,51,54] Entheses were loaded at 3% cyclic tension at a physiological strain rate (1 Hz), and videos of loading cycles were recorded for n = 6 samples (Movies 7−12). Peak-to-peak strain maps were created from videos using the digital image correlation software[19,55] and spatially correlated with data from Raman images using features of the mineralized tissue visible in both confocal fluorescence and Raman images (Figure 2b,c). Visual analysis of strain maps reveals that strains are highly localized to the soft tissue, consistent with the fact that the bone has a much higher modulus than the soft tissue. Furthermore, we observed the presence of highly localized strains between the fibers in areas situated away from the mineralized interface (Figure 4a−c). We also observed a multiple order of magnitude increase in peak-to-peak strain magnitude moving away from the mineralized interface, evident by a logarithmic trend in strain magnitude (Figure 4d). As the compositional variation within this region does not account for this logarithmic increase in strain (Figure 2c), structural considerations within the unmineralized region of the enthesis must significantly affect mechanical behavior.

Structural data (Figure 3) indicates that the collagen in the soft tissue undergoes a change from disorganized bundles to oriented fibers moving away from the mineralized interface. Spatially, correlating the mechanical data with the structural data, we observe that the strains in the disorganized bundle region (UM.1) occur at magnitudes similar to the applied strain, meaning that the mineral/matrix gradient can appropriately mediate strains into the mineralized tissue. Qualitative examination of loading movies indicates that within the region of the oriented fibers (UM.2), strains originate from fiber movements (Figure 4a,b, Supporting Information, Figure S9). During loading, fibers can be observed moving with respect to one another, rather than moving as a unit (Movies 7−12). This behavior indicates that the fibers are only loosely bound to each other, thereby allowing for them to move individually, as we see deformations within the tissue that do not entirely result from strains within the fibers themselves (Figure 4a,b). These observations indicate that the fibers are primarily translating and rotating, rather than stretching, thus, allowing for large displacements to occur without localizing strain to the disorganized bundle region (UM.1). Given that strains in the region of the oriented fibers region arise from structural considerations, such as the

DOI: 10.1021/acsami.9b03595
ACS Appl. Mater. Interfaces 2019, 11, 26559−26570

allowance for fiber translations and rotations, we have termed them "structural strains", thereby, differentiating them from material strains.

To connect the size of these mechanical regions with the structural changes we observed, we analyzed where the structural strains begin to dominate the mechanical behavior of the tissue. Quantitative measurement of this transition was performed by normalizing strain as a function of distance from the mineralized interface to the average global strain of the strain map of each sample. The point at which the average strain increased above the global strain was determined as the transition location (Supporting Information, Figure S10). This value was found to occur 1310 ± 506 μm from the mineralized interface, matching closely with the value recorded for the structurally derived disorganized bundle region (1008 ± 367 μm). The sizes of these regions agree, indicating that the onset of the high structural strains arises from oriented fibers. Further, given that the strain maps were derived from samples under tension, we know that the disorganized bundle region (UM.1) must transfer load. Therefore, we theorize that this region (UM.1) is more homogeneously structured than the heterogeneously organized oriented fibers region (UM.2). These data suggest that the strains in the disorganized bundle region (UM.1) are material strains, whereas those in the region of oriented fibers (UM.2) are primarily structural strains. Given the inverse relationship of strain and stiffness, our mechanical analysis indicates that the mineralized region (M) is much stiffer than the unmineralized region (UM), and that the unmineralized tissue is mechanically comprised of a homogeneous compliant region and a heterogeneous compliant region corresponding to disorganized bundles (UM.1) and oriented fibers (UM.2), respectively.

Enthesis Combines Structure and Composition To Provide Mobility within the Tissue without Localizing Strain at the Interface. Probing the tissue at a length scale that matches the morphological variations observed through histology allowed us to compare and localize composition, structure, and mechanics in the meniscal enthesis (Figure 5). We were able to spatially correlate these aspects of the tissue by aligning regions we observed to be present in our Raman and mechanical analyses, namely, the interface between mineralized and unmineralized tissues (Figure 2b,c). Compositionally, we observed a shift from mineralized (M) to unmineralized (UM) tissue through a gradient in mineral/matrix ratio, similar to mineral/matrix gradients observed in other entheses found throughout the body.[17,26,30,31] The mineralized portion of the enthesis contains three distinct structural regions (M.1, M.2, M.3) that result in a mechanically stiff region, indicating that this mechanical transition is driven by compositional changes at physiologic loads. Hypothetically, structural changes in the mineralized tissue of the enthesis also relate to local changes in mechanical behavior related to porous and dense bone, but further measurements under non-physiologic loading conditions would be required to explicitly measure these changes. The unmineralized portion of the enthesis possesses two structural regions (UM.1, UM.2) that each result in different mechanical behavior, meaning that the structure drives the mechanics within the unmineralized tissue (UM) at physiologically relevant loads.[23,56] Previous studies have hypothesized that the mineral/matrix gradient in addition to localized stiffness changes near the interface contribute to the strengthening of the interface between the soft tissue and bone at the microscale.[18,20,30,31,57] For the first time, we demonstrate a new mechanical mechanism, fiber sliding within the soft tissue regions of this interface, and spatially correlate it with a full picture of the structuring across the meniscal enthesis.

We further postulate that these structurally defined regions play individual roles pertaining to the bulk mechanics of the enthesis. The oriented fibers (UM.2) of the heterogeneous compliant region permit large displacements to occur within the tissue in the form of structural strains due to fiber sliding. We propose that this sliding phenomenon allows for lateral movement of the meniscus without resulting in the high strains this type of motion would impart into the interface between mineralized and unmineralized tissues. The oriented fiber region transitions into the disorganized bundles (UM.1) of the homogeneous compliant region, which only allows for smaller material strains. This region likely corresponds to the splayed fibers previously identified in tendon entheses. We found that the strain magnitude within this region logarithmically decreases prior to the transition into the mineralized tissue (M) (Figure 4d), which is consistent with previous hypotheses regarding fiber splaying in the enthesis.[16] Within the mineralized tissue, previous mechanical studies on human meniscal entheses using nanoindentation indicate that a logarithmic increase in stiffness occurs within the first few hundred microns moving into the mineralized tissue.[20] Extrapolating this information onto our data implies that the logarithmic strain response we observed would extend into the mineralized tissue. We suggest that the mineral/matrix gradient, marking the beginning of this stiffness increase in the mineralized tissue, is of sufficient length to transition the relatively low strains observed near the interface between mineralized and unmineralized tissues to the further mineralized regions. Subsequently, within the mineralized tissue, the transitional region (M.3) appears to provide a laterally continuous area of attachment for the disorganized bundles (UM.1). The location of the transitional region (M.3) is morphologically consistent with the calcified fibrocartilage, as evidenced by the presence of chondrocyte lacunae visible in confocal fluorescence images (Figures 2a,b and 3a,b). Past the transitional region (M.3), a gradient in porosity from dense trabeculae (M.2) to open trabeculae (M.1) blends the interfacial tissue with the subchondral bone (Figure 5). The porosity in these regions provides a location for the bone marrow to reside but also decreases the bulk tissue stiffness, as the bone marrow has a much lower stiffness than the bone.

The picture emerges that the oriented fibers (UM.2) of the enthesis provide the meniscus with mobility for its role as a shock absorber, localizing the high displacements required for the meniscus to function to this region (UM.2). The disorganized bundles (UM.1) splay into the mineralized tissue[16] and distribute load through a logarithmic decrease in strain. The transitional region (M.3) marks the onset of mineralized tissue and provides a laterally continuous region of insertion for the disorganized bundles. The start of the transitional region coincides with a local mineral/matrix gradient, interfacing the mineralized and unmineralized tissues before showing a continuing gradient in stiffness extending into the mineralized tissue.[20] The end of the transitional region (M.3) corresponds to the onset of porous tissue, providing a gradual structural transition into subchondral bone, while simultaneously softening the stiffness gradient at a bulk tissue scale. To extend the structures and mechanisms to other engineered systems or mechanical models, we would need to

DOI: 10.1021/acsami.9b03595
ACS Appl. Mater. Interfaces 2019, 11, 26559−26570

calculate local elastic moduli for each of these regions. Coupling our data with values from previous works, we can speculate that a change in the stiffness of the oriented fibers (UM.2) (10−100 MPa)[20,27] should undergo a logarithmic increase moving through the disorganized bundles (UM.1) within the soft tissue regions. After which the tissue possesses a gradient in mineral/matrix content (1−10 GPa),[20,58,59] before reaching the stiffness of calcified cartilage in the transitional region (M.3) and finally to bone (∼20 GPa)[22] within the remaining mineralized regions (M.1, M.2). These values represent the local material stiffnesses. While these stiffness values are important with regard to binding soft tissue and bone, we emphasize that structure also plays an important role in enthesis functionality.

This work also provides insight into the nanoscale aspects of the enthesis. As we believe the disorganized bundles region (UM.1) corresponds to the splaying of fibers identified in other entheses,[16] we suggest that the difference in mechanical behavior observed between the disorganized bundles (UM.1) and oriented fibers (UM.2) relates to the nanoscale structuring of the collagen in these regions. Previous studies have found that the fibers of ligaments, tendons, etc. consist of type I collagen, whereas the tissue near the interface between soft tissue and bone is largely type II collagen.[16,25] These collagens self-assemble into fibrils of different sizes based on their type, where type I collagen assembles into fibrils of larger diameters (100s of nanometers) than type II collagen (10s of nanometers).[60,61] The apparent disorganized nature of the disorganized bundles (UM.1) may result from the collagen fibril type within this region, where these structures are organized at the nanoscale but disorganized at the microscale. Conversely the type I collagen results in larger fibrils, generating the microscale organization observed in the region of oriented fibers (UM.2). Collagen organization may have further connotations in the location of mineral with respect to collagen across the mineral gradient near the transitional region (M.3). The distribution of the mineral with respect to the collagen fibrils has been shown to be different at the nanoscale, where the mineral is largely contained within the interior of collagen fibrils in the bone and exterior to fibrils farther along the gradient.[62] Disorganized collagen bundles may allow for the increased presence of mineral exterior to collagen fibrils. Further, different concentrations of biomolecules associated with collagen cross-linking have been found near the insertion versus the bulk of the enthesis.[16] These data may explain the fiber sliding phenomena we observed within the region of oriented fibers (UM.2) versus the disorganized bundles (UM.1), which we found to be necessary for enthesis function. These nanoscale considerations may relate to the overall mechanics of the enthesis, given that we find evidence for a direct relationship between the structure and mechanics of the enthesis within the soft tissue regions.

In addition to the nano- and microscale features we have identified, larger scale features in the lateral directions, including interdigitation between mineralized and unmineralized tissues[63] and between the calcified fibrocartilage and bone,[20] also provide further toughening mechanisms by interlocking these tissues and providing an increased surface area.[63] These structural features act in concert to allow for large displacements within the enthesis without localizing strains to the interface between mineralized and unmineralized tissues, thus, minimizing the presence of stress concentrators between these mechanically dissimilar materials.

Our analysis of the enthesis was performed on neonatal tissues, which are still developing. Although these structures are functional, the size and/or presence of these regions may change as the animals age. However, this study represents the first of its kind to analyze the enthesis at this length scale, ranging from the trabecular bone of the tibia to the oriented fibers of the ligamentous tissue in the meniscal insertion. Although few analyses have approached the construction of the enthesis as it is addressed here, other studies have recognized similar features to the structures we observed. For example, a gradient in collagen organization and alignment was found moving from the tendon to bone, likely highlighting similar regions to the two structural regions we termed disorganized bundles (UM.1) and oriented fibers (UM.2).[31] Based on our own observations and those from other studies, we believe that these regions will remain present throughout the development of the animals.[25,26,64] However, we speculate that some of these regions, particularly, the disorganized bundles (UM.1), will shrink as the animal ages. In this framework, the oriented fibers (UM.2) will begin to extend closer to the mineral gradient between mineralized and unmineralized tissues during aging, eventually directly representing the splayed fibers previously identified.[16,20] Therefore, the large size of the disorganized bundle region (UM.1) we observed in these samples may be a developmental aspect of the enthesis, possibly indicating its importance when engineering such structures.

CONCLUSIONS

Here, we have outlined a full view of the structure of the enthesis, from the bone to oriented fibers in the bulk of the attachment and correlated this structure with the mechanical phenomena that aid in interfacial robustness. Our data indicates that a robust soft tissue-to-bone interface requires three components: mobile fiber units, a continuous interfacial region, and a local stiffness gradient. Working in concert, these components gradually dissipate stresses without localizing stresses at the edges of pores, between fibers, etc. These findings elucidate the mechanisms that prevent the buildup of stress concentrators at the soft tissue-to-bone interface while providing extensive mobility within the soft tissue. Implementing these mechanisms in engineered constructs has the potential to inform the production of interfacial tissue implants and biomimetic materials junctions. Although a high degree of focus has been placed on generating stiffness gradients for interfacial engineering, our work shows that structural features within the soft portions of the attachment are also necessary for the interface function. Specifically, the presence of fibers allows for lateral movement with respect to the interface, which is particularly important to the meniscal function. More attention should be paid to the development of hierarchical fiber arrangements in future designs.[6,9,65−67] Future work should focus on examining the fibrillar structure of the collagen in the soft tissue regions of the enthesis. Understanding the mechanisms by which the enthesis assembles differently structured but interconnected soft tissue regions would greatly aid in our ability to construct similarly robust interfaces. Further, by comparing the enthesis system to other biological interfaces, such as the mussel byssus or the sutures of turtle shells,[68−70] we can identify whether nature has converged on similar mechanistic principles for connecting soft and hard materials. Overall, these data can be used to inform the design and fabrication of interfaces between dissimilar material

DOI: 10.1021/acsami.9b03595
ACS Appl. Mater. Interfaces 2019, 11, 26559−26570

systems by utilizing the structural framework provided through our analysis of the enthesis and dialing in appropriate moduli for the application. These principles, learned from the construction of the enthesis, constitute a new paradigm for producing robust interfaces in artificial tissues, robotics, prosthetics, and other engineered systems.

METHODS

Tissue Acquisition and Preparation. Enthesis samples were explanted from 1 to 3 day old neonatal bovine legs from 12 different animals (6 for Raman analysis and 6 for mechanical analysis) (Gold Medal Packing Inc.). The medial caudal meniscal enthesis was chosen, as it is the most commonly injured enthesis in the human knee joint.[71] Bovine stifle joints were disarticulated, and samples were removed from the center of the enthesis by making cuts parallel to the fibers. These samples were immediately frozen and embedded in Optimum Cutting Temperature compound (Tissue-Tek). Blocks were shaved using a cryostat (Thermo Scientific Mircom HM 550), until the bone and ligamentous tissue interface was visible on the tissue block. Resulting blocks were unfrozen immediately prior to analysis by Raman microscopy or confocal elastography.

Histology. Enthesis samples were explanted in the same manner, as described above. However, instead of cryosectioning, samples were fixed in formalin, decalcified, and embedded in paraffin. Sections were taken at 4 μm thickness and stained with Weigart's hematoxylin (Amresco) for 10 min and Picrosirius Red (Rowley Biochemical Inc.) for 1 h. Slides were imaged on a microscope (Nikon Eclipse TE2000-S) through an attached camera (Diagnostic Instruments, Inc. RTKE Spot) in white light and under cross-polarized light.

Raman Microscopy. Raman analysis was performed for n = 6 samples. Tissue samples were thawed and glued to a Petri dish before submersion in PBS. Raman imaging (Renishaw InVia Confocal Raman microscope) was performed immediately after thawing. Raman spectra were collected using a 532 nm laser (Cobalt Samba 500 DPSS Laser System) through a water immersion objective lens that was also submerged in PBS with the sample. 10× (Leica, NA 0.30) and 63× (Leica, NA 0.90) dipping lenses were utilized for mapping and collection of individual spectra, respectively. For mapping, spectra were collected using a ~4 × 0.5 mm^2 grid at a 25 μm step size as the laser spot size was determined to be ~25 μm in diameter. Laser power was set to 200 mW and collected with a 1 s integration time through a 600 l/mm grating on a charge-coupled device detector.

Raman images representative of a given biological component were generated using characteristic peak areas that had minimal overlap with other components present in the meniscal enthesis: apatite (950−980 cm^{-1}), collagen (833−905, 1224−1296, 1439−1484, 2908−3028 cm^{-1}), and lipid (1278−1326, 1423−1468, 2835−2870 cm^{-1}).[72,73] Area maps were converted to text image format and further processed using FIJI.[74] To reduce the noise and enhance the image quality, all images of the peak area for a given component were summed (with the exception of apatite). Final component images for collagen, apatite, and lipids were stacked and processed as image composites with LUTs assigned to the components (apatite: yellow; collagen: red; lipid: cyan). The minimum was set to zero for each component, and maximum intensity values were adjusted to both eliminate saturated pixels and ensure simultaneous visualization of the given components (apatite: 0−13 900, collagen: 0−144 000, lipid: 0−60 600). The final composite image was converted to 24-bit red−green−blue for portability and compatibility (Figure 2a and Supporting Information, Figure S3).

Peak areas and peak area ratios for compositional and structural analyses were calculated using the Renishaw WiRE 4 Software. All negative peak areas were replaced with zeros, since a negative calculated peak area indicates the lack of a peak. The mineral/matrix ratio was calculated using the ratio of the $\nu_1PO_4^{3-}$ band to the amide III band and was defined as 950−980/1224−1296 cm^{-1}. A ratio of these bands was chosen to allow for comparison between samples. Due to the opacity of bone, the measurement of composition using a single peak can be challenging.[52,53] Further plotting of maps, averaging of maps, histogram-based analysis, and FFT-based analysis were performed using Mathematica. Maps were plotted and averaged as a function of distance from the interface to measure the length of the mineral/matrix gradient (Figure 2c and Supporting Information, Figure S4). The start of the gradient was empirically defined as a mineral/matrix ratio of 2 occurring before the interface, sloping to a value of less than 0.1, which was defined as the end of the gradient region.

Structural collagen maps were produced by mapping the 2908−3028 cm^{-1} peak area (Supporting Information, Figure S5). The distribution of peak area values for each map was divided into even quintiles, and the maps were replotted using these quintiles to normalize data across samples (Figure 3a,b and Supporting Information, Figure S6). Quantiles were empirically established for distinguishing pores and changes related to the topological distribution of fibers. Quintile division was found to follow closest to empirically established quantiles without requiring the division of the distribution using uneven quantiles. Therefore, the quintile division of CH peak complex area distribution was used to facilitate the analysis of collagen structuring data (Supporting Information, Figure S7). Maps were spatially binned into 200 μm (8 pixel) wide columns beginning in the soft tissue regions of the enthesis and extended back to the bony regions. Histograms of the quintile values in these grids were produced and analyzed to determine textural changes in collagen. Fingerprints of different regions were identified from these histograms and used to determine changes in the structure from quintile plots.

The analysis of orientation was performed using FFTs. A region one-third of the size of the distance from the transitional region (M.3) to the end of the image was utilized as a sliding window to measure orientation using FFTs. The pixels of this window were first linearly interpolated, and a Hann Window function, fitted to the dimensions of the window, was applied to remove artifacts arising from boundary effects (Supporting Information, Figure S8).[75] Two-dimensional FFTs were calculated for this window, and 2D FFTs were cropped to only contain the center 50 × 50 pixel area (low-frequency area). These images were then thresholded to remove pixels with intensities below 0.5; the range of pixel intensities in each 2D FFT is from 0 to 1. Images were rotated in 5° increments, and center two rows of pixels were averaged. Maximum average pixel intensity was calculated as a function of angle. This value was then divided by the average pixel intensity at the angle orthogonal to the angle with the maximum average pixel intensity and used as an orientation index. These values were plotted, and the peak in the plot was determined as the onset of the oriented tissue (Supporting Information, Movies 1−6 and Figure S6).

Confocal Fluorescence Elastography. Strain analysis was performed for n = 6 samples. Samples were stained with 5-DTAF (ex/em 492/516 nm, Invitrogen), a general protein stain, for 60 min and prestressed at 3 kPa for 30 min in PBS, calculated by measuring the cross-sectional area of the bony portion of the enthesis tissue block. Samples were mounted into a piezoelectrically actuated microload frame with a hydration dish containing PBS.[48,51,54] The microload frame was placed on an inverted confocal microscope (LSM 5 LIVE, Carl Zeiss Inc.) and imaged using a 10× objective and a 488 nm laser. Samples were cyclically strained in tension at a 3% peak-to-peak strain, defined as the total strain applied from the minimum strain in a sinusoid to the maximum strain in a sinusoid, at 1 Hz around the gauge length of the soft tissue of the sample (measured at the conclusion of prestressing). Confocal slice thicknesses were ~10−20 μm. Videos of loading cycles were recorded at 20 frames/s using a high-speed camera (v7.1, Vision Research). Videos were analyzed using FIJI to determine the start of the loading cycle.[74] Frame 10 was used as the peak of the sinusoidal loading cycle. The Ncorr digital image correlation code, run through MATLAB, was used to develop spatially correlated strain maps.[55] For this analysis, the reference configuration was defined as the first frame in the loading video, and the deformed configurations consisted of the following frames in the video of the loading cycle. A subset radius of

DOI: 10.1021/acsami.9b03595
ACS Appl. Mater. Interfaces 2019, 11, 26559−26570

15 with a subset spacing of 5 and a correlation coefficient of 1.2 was used in the Ncorr software. E_{xx}, E_{yy}, and E_{xy} Langrangian finite strain maps were developed for each sample. These maps were concatenated into a single, stitched map of the entire enthesis region. These data were loaded into *R* for analysis. The interface with the mineralized tissue was visually identified, and data prior to that interface was removed. Resulting strain maps were collapsed into average strain as a function of distance from the calcified interface. These data were binned in the direction of the interface. Variance and standard deviation were calculated from the initial strain maps and binned in the same manner. To determine the length of the homogeneous compliant region, the average strain for the entire map was calculated, and average strains as a function of distance were normalized to this value. The point at which the normalized strain increased above 1 was considered the point at which structural strains dominated the tissue's mechanical behavior. To generate semilog plots, the absolute value of the average data from above was taken, and the log of that value was calculated. These data were plotted as a function of distance from the mineralized interface.

Image Display. To reduce the effects of stitching in confocal fluorescence images (Figure 2b), image transparency was decreased to 60%, and stitched images were placed on the top of each other. Resulting stitched image transparency was again decreased to 75% and placed over a black background. For the remaining confocal fluorescence images, transparency was reduced to 75% and placed over a black background (Figure 4a and Supporting Information, Figure S9). Brightness and contrast for confocal fluorescence images used in movies (Supporting Information, Movies 7−12) were autoadjusted using FIJI.[74]

■ ASSOCIATED CONTENT

Supporting Information

The Supporting Information is available free of charge on the ACS Publications website at DOI: 10.1021/acsami.9b03595.

Explant of the medial caudal meniscal enthesis; Raman spectra of different regions of the enthesis; composite Raman peak area maps; raw CH peak complex; quintile images with histogram analysis; descriptive captions for Movies 1−12 (PDF)

Orientation index plot for sample I with the corresponding FFT stack (AVI)

Orientation index plot for sample II with the corresponding FFT stack (AVI)

Orientation index plot for sample III with the corresponding FFT stack (AVI)

Orientation index plot for sample IV with the corresponding FFT stack (AVI)

Orientation index plot for sample V with the corresponding FFT stack (AVI)

Orientation index plot for sample VI with the corresponding FFT stack (AVI)

Load cycle for sample VIII with the corresponding $E[xx]$ tensile strain map and plot (AVI)

Load cycle for sample VII (AVI)

Load cycle for sample IX (AVI)

Load cycle for sample X (AVI)

Load cycle for sample XI (AVI)

Load cycle for sample XII (AVI)

■ AUTHOR INFORMATION

Corresponding Author

*E-mail: lb244@cornell.edu.

ORCID

Alexander J. Boys: 0000-0002-6488-7005

Jennie A. M. R. Kunitake: 0000-0002-7061-3211

Lara A. Estroff: 0000-0002-7658-1265

Author Contributions

A.J.B. performed all experiments and majority of data analysis, assembled all figures, and wrote the manuscript. J.A.M.R.K. assisted in Raman analysis, specifically compositional analysis, and production of composite Raman images. J.A.M.R.K. also assisted in the development of Raman testing procedures. C.R.H. assisted in the development of mechanical testing procedures. I.C. assisted in data interpretation. L.A.E. and L.J.B. supervised the planning of experiments, directed research, and assisted in data interpretation. All authors revised and reviewed the manuscript.

Notes

The authors declare no competing financial interest.

■ ACKNOWLEDGMENTS

The authors acknowledge Dr. Shefford Baker for his assistance in interpreting data for this work. A.J.B. acknowledges a predoctoral fellowship award (F31AR070009) from the National Institute of Arthritis and Musculoskeletal and Skin Diseases (NIAMS) of the National Institutes of Health (NIH). The content is solely the responsibility of the authors and does not necessarily represent the official views of the National Institutes of Health. We also acknowledge Cornell Center for Materials Research (CCMR) under DMR-1719875 for instrument usage and the Cornell University College of Veterinary Medicine for histological embedding and sectioning. Partial support for this research came from the National Cancer Institute of the National Institutes of Health under award number R01CA173083. The authors would also like to acknowledge grants NSF 1536463 and NSF 1807602.

■ ABBREVIATIONS

5-DTAF, 5-(4,6-dichlorotriazinyl) aminofluorescein
FFT, fast Fourier transform
PBS, phosphate-buffered saline

■ ADDITIONAL NOTE

[a]Tissue regions are identified parenthetically by number throughout the manuscript and in figures for clarity and consistency. Regions numbered (M.1), (M.2), etc. fall within the region (M) and so on.

■ REFERENCES

(1) Gupta, P.; Adhikary, M.; Christakiran, J. M.; Kumar, M.; Bhardwaj, N.; Mandal, B. B. Biomimetic, Osteoconductive Non-Mulberry Silk Fiber Reinforced Tricomposite Scaffolds for Bone Tissue Engineering. *ACS Appl. Mater. Interfaces* **2016**, *8*, 30797−30810.

(2) Chen, G.; Dong, C.; Yang, L.; Lv, Y. 3D Scaffolds with Different Stiffness but the Same Microstructure for Bone Tissue Engineering. *ACS Appl. Mater. Interfaces* **2015**, *7*, 15790−15802.

(3) Chen, C.; Liu, F.; Tang, Y.; Qu, J.; Cao, Y.; Zheng, C.; et al. Book-Shaped Acellular Fibrocartilage Scaffold with Cell-Loading Capability and Chondrogenic Inducibility for Tissue-Engineered Fibrocartilage and Bone-Tendon Healing. *ACS Appl. Mater. Interfaces* **2019**, *11*, 2891−2907.

(4) Bhattacharjee, M.; Chameettachal, S.; Pahwa, S.; Ray, A. R.; Ghosh, S. Strategies for Replicating Anatomical Cartilaginous Tissue Gradient in Engineered Intervertebral Disc. *ACS Appl. Mater. Interfaces* **2014**, *6*, 183−193.

(5) Boys, A. J.; Zhou, H.; Harrod, J.; McCorry, M. C.; Estroff, L. A.; Bonassar, L. J. Top-down Fabrication of Spatially Controlled Mineral-

Gradient Scaffolds for Interfacial Tissue Engineering. *ACS Biomater. Sci. Eng.* **2019**, *5*, 2988−2997.
(6) Font Tellado, S.; Bonani, W.; Rosado Balmayor, E.; Föhr, P.; Motta, A.; Migliaresi, C.; van Griensven, M. Fabrication and Characterization of Biphasic Silk Fibroin Scaffolds for Tendon/Ligament-to-Bone Tissue Engineering. *Tissue Eng., Part A* **2017**, *23*, 859−872.
(7) Liu, Y.; Thomopoulos, S.; Chen, C.; Birman, V.; Buehler, M. J.; Genin, G. M. Modelling the Mechanics of Partially Mineralized Collagen Fibrils, Fibres and Tissue. *J. R. Soc., Interface* **2013**, *11*, No. 20130835.
(8) Lipner, J. H.; Liu, W.; Liu, Y. X.; Boyle, J. J.; Genin, G. M.; Xia, Y.; Thomopoulos, S. The Mechanics of PLGA Nanofiber Scaffolds with Biomimetic Gradients in Mineral for Tendon-to-Bone Repair. *J. Mech. Behav. Biomed. Mater.* **2014**, *40*, 59−68.
(9) McCorry, M. C.; Mansfield, M. M.; Sha, X.; Coppola, D. J.; Lee, J. W.; Bonassar, L. J. A Model System for Developing a Tissue Engineered Meniscal Enthesis. *Acta Biomater.* **2017**, *56*, 110−117.
(10) Spalazzi, J. P.; Doty, S. B.; Moffat, K. L.; Levine, W. N.; Lu, H. H. Development of Controlled Matrix Heterogeneity on a Triphasic Scaffold for Orthopedic Interface Tissue Engineering. *Tissue Eng.* **2006**, *12*, 3497−3508.
(11) Iannucci, L. E.; Boys, A. J.; McCorry, M. C.; Estroff, L. A.; Bonassar, L. J. Cellular and Chemical Gradients to Engineer the Meniscus-to-Bone Insertion. *Adv. Healthcare Mater.* **2019**, No. 1800806.
(12) Bartlett, N. W.; Tolley, M. T.; Overvelde, J. T. B.; Weaver, J. C.; Mosadegh, B.; Bertoldi, K.; Whitesides, G. M.; Wood, R. J. A 3D-Printed, Functionally Graded Soft Robot Powered by Combustion. *Science* **2015**, *349*, 161−165.
(13) Miserez, A.; Schneberk, T.; Sun, C.; Zok, F. W.; Waite, J. H. The Transition from Stiff to Compliant Materials in Squid Beaks. *Science* **2008**, *319*, 1816−1819.
(14) Boys, A. J.; McCorry, M. C.; Rodeo, S. A.; Bonassar, L. J.; Estroff, L. A. Next Generation Tissue Engineering of Orthopedic Soft Tissue-to-Bone Interfaces. *MRS Commun.* **2017**, *7*, 289−308.
(15) Bonnevie, E. D.; Mauck, R. L. Physiology and Engineering of the Graded Interfaces of Musculoskeletal Junctions. *Annu. Rev. Biomed. Eng.* **2018**, *20*, 403−429.
(16) Rossetti, L.; Kuntz, L. A.; Kunold, E.; Schock, J.; Grabmayr, H.; Sieber, S. A.; Burgkart, R. H.; Bausch, A. R.; et al. The Microstructure and Micromechanics of the Tendon−Bone Insertion. *Nat. Mater.* **2017**, *16*, 664−670.
(17) Schwartz, A. G.; Pasteris, J. D.; Genin, G. M.; Daulton, T. L.; Thomopoulos, S. Mineral Distributions at the Developing Tendon Enthesis. *PLoS One* **2012**, *7*, No. e48630.
(18) Deymier, A. C.; An, Y.; Boyle, J. J.; Schwartz, A. G.; Birman, V.; Genin, G. M.; Thomopoulos, S.; Barber, A. H. Micro-Mechanical Properties of the Tendon-to-Bone Attachment. *Acta Biomater.* **2017**, *56*, 25−35.
(19) Spalazzi, J. P.; Gallina, J.; Fung-Kee-Fung, S. D.; Konofagou, E. E.; Lu, H. H. Elastographic Imaging of Strain Distribution in the Anterior Cruciate Ligament and at the Ligament−Bone Insertions. *J. Orthop. Res.* **2006**, *24*, 2001−2010.
(20) Abraham, A. C.; Haut Donahue, T. L. From Meniscus to Bone: A Quantitative Evaluation of Structure and Function of the Human Meniscal Attachments. *Acta Biomater.* **2013**, *9*, 6322−6329.
(21) Khetia, E. A.; McKeon, B. P. Meniscal Allografts: Biomechanics and Techniques. *Sports Med. Arthrosc. Rev.* **2007**, *15*, 114−120.
(22) Weiner, S.; Wagner, H. D. THE MATERIAL BONE: Structure-Mechanical Function Relations. *Annu. Rev. Mater. Sci.* **1998**, *28*, 271−298.
(23) Joshi, M. D.; Suh, J. K.; Marui, T.; Woo, S. L. Interspecies Variation of Compressive Biomechanical Properties of the Meniscus. *J. Biomed. Mater. Res.* **1995**, *29*, 823−828.
(24) Messner, K.; Gao, J. The Menisci of the Knee Joint. Anatomical and Functional Characteristics, and a Rationale for Clinical Treatment. *J. Anat.* **1998**, *193*, 161−178.
(25) Gao, J. Immunolocalization of Types I, II, and X Collagen in the Tibial Insertion Sites of the Medial Meniscus. *Knee Surg., Sports Traumatol. Arthrosc.* **2000**, *8*, 61−65.
(26) Spalazzi, J. P.; Boskey, A. L.; Pleshko, N.; Lu, H. H. Quantitative Mapping of Matrix Content and Distribution across the Ligament-to-Bone Insertion. *PLoS One* **2013**, *8*, No. e74349.
(27) Villegas, D. F.; Maes, J. A.; Magee, S. D.; Haut Donahue, T. L. Failure Properties and Strain Distribution Analysis of Meniscal Attachments. *J. Biomech.* **2007**, *40*, 2655−2662.
(28) Hauch, K. N.; Villegas, D. F.; Haut Donahue, T. L. Geometry, Time-Dependent and Failure Properties of Human Meniscal Attachments. *J. Biomech.* **2010**, *43*, 463−468.
(29) Wopenka, B.; Kent, A.; Pasteris, J. D.; Yoon, Y.; Thomopoulos, S. The Tendon-to-Bone Transition of the Rotator Cuff: A Preliminary Raman Spectroscopic Study Documenting the Gradual Mineralization across the Insertion in Rat Tissue Samples. *Appl. Spectrosc.* **2008**, *62*, 1285−1294.
(30) Deymier-Black, A. C.; Pasteris, J. D.; Genin, G. M.; Thomopoulos, S. Allometry of the Tendon Enthesis: Mechanisms of Load Transfer Between Tendon and Bone. *J. Biomech. Eng.* **2015**, *137*, No. 111005.
(31) Genin, G. M.; Kent, A.; Birman, V.; Wopenka, B.; Pasteris, J. D.; Marquez, P. J.; Thomopoulos, S. Functional Grading of Mineral and Collagen in the Attachment of Tendon to Bone. *Biophys. J.* **2009**, *97*, 976−985.
(32) Sherman, V. R.; Yang, W.; Meyers, M. A. The Materials Science of Collagen. *J. Mech. Behav. Biomed. Mater.* **2015**, *52*, 22−50.
(33) Genin, G. M.; Thomopoulos, S. The Tendon-to-Bone Attachment: Unification through Disarray. *Nat. Mater.* **2017**, *16*, 607−608.
(34) Amini, S.; Masic, A.; Bertinetti, L.; Teguh, J. S.; Herrin, J. S.; Zhu, X.; Su, H.; Miserez, A. Textured Fluorapatite Bonded to Calcium Sulphate Strengthen Stomatopod Raptorial Appendages. *Nat. Commun.* **2014**, *5*, No. 3187.
(35) Bi, X.; Patil, C. A.; Lynch, C. C.; Pharr, G. M.; Mahadevan-Jansen, A.; Nyman, J. S. Raman and Mechanical Properties Correlate at Whole Bone- and Tissue-Levels in a Genetic Mouse Model. *J. Biomech.* **2011**, *44*, 297−303.
(36) Bergholt, M. S.; St-Pierre, J.-P.; Offeddu, G. S.; Parmar, P. A.; Albro, M. B.; Puetzer, J. L.; Oyen, M. L.; Stevens, M. M. Raman Spectroscopy Reveals New Insights into the Zonal Organization of Native and Tissue-Engineered Articular Cartilage. *ACS Cent. Sci.* **2016**, *2*, 885−895.
(37) Albro, M. B.; Bergholt, M. S.; St-Pierre, J.-P.; Vinals Guitart, A.; Zlotnick, H. M.; Evita, E. G.; Stevens, M. M. Raman Spectroscopic Imaging for Quantification of Depth-Dependent and Local Heterogeneities in Native and Engineered Cartilage. *Regener. Med.* **2018**, *3*, No. 3.
(38) Asiala, S. M.; Shand, N. C.; Faulds, K.; Graham, D. Surface-Enhanced, Spatially Offset Raman Spectroscopy (SESORS) in Tissue Analogues. *ACS Appl. Mater. Interfaces* **2017**, *9*, 25488−25494.
(39) Ortgies, D. H.; de la Cueva, L.; del Rosal, B.; Sanz-Rodríguez, F.; Fernández, N.; Iglesias-de la Cruz, M. C.; Salas, G.; Cabrera, D.; Teran, F. J.; Jaque, D.; et al. In Vivo Deep Tissue Fluorescence and Magnetic Imaging Employing Hybrid Nanostructures. *ACS Appl. Mater. Interfaces* **2016**, *8*, 1406−1414.
(40) *Infrared and Raman Spectroscopic Imaging*, 2nd ed.; Salzer, R.; Siesler, H. W., Eds.; Wiley-VCH: Weinheim, Germany, 2014.
(41) Zavaleta, C. L.; Smith, B. R.; Walton, I.; Doering, W.; Davis, G.; Shojaei, B.; Natan, M. J.; Gambhir, S. S. Multiplexed Imaging of Surface Enhanced Raman Scattering Nanotags in Living Mice Using Noninvasive Raman Spectroscopy. *Proc. Natl. Acad. Sci. U.S.A.* **2009**, *106*, 13511−13516.
(42) Akiva, A.; Kerschnitzki, M.; Pinkas, I.; Wagermaier, W.; Yaniv, K.; Fratzl, P.; Addadi, L.; Weiner, S. Mineral Formation in the Larval Zebrafish Tail Bone Occurs via an Acidic Disordered Calcium Phosphate Phase. *J. Am. Chem. Soc.* **2016**, *138*, 14481−14487.

DOI: 10.1021/acsami.9b03595
ACS Appl. Mater. Interfaces 2019, 11, 26559−26570

(43) Gamsjaeger, S.; Klaushofer, K.; Paschalis, E. P. Raman Analysis of Proteoglycans Simultaneously in Bone and Cartilage. *J. Raman Spectrosc.* **2014**, *45*, 794−800.
(44) Mansfield, J. C.; Moger, J.; Green, E.; Moger, C.; Winlove, C. P. Chemically Specific Imaging and In-Situ Chemical Analysis of Articular Cartilage with Stimulated Raman Scattering. *J. Biophotonics* **2013**, *6*, 803−814.
(45) Kammer, M.; Hedrich, R.; Ehrlich, H.; Popp, J.; Brunner, E.; Krafft, C. Spatially Resolved Determination of the Structure and Composition of Diatom Cell Walls by Raman and FTIR Imaging. *Anal. Bioanal. Chem.* **2010**, *398*, 509−517.
(46) Adie, S. G.; Liang, X.; Kennedy, B. F.; John, R.; Sampson, D. D.; Boppart, S. A. Spectroscopic Optical Coherence Elastography. *Opt. Express* **2010**, *18*, 25519−25534.
(47) Rey-De-Pedraza, V.; Cendon, D. A.; Sánchez-Gálvez, V.; Gálvez, F. Measurement of Fracture Properties of Concrete at High Strain Rates. *Philos. Trans. R. Soc., A* **2017**, *375*, No. 20160174.
(48) Buckley, M. R.; Gleghorn, J. P.; Bonassar, L. J.; Cohen, I. Mapping the Depth Dependence of Shear Properties in Articular Cartilage. *J. Biomech.* **2008**, *41*, 2430−2437.
(49) Silverberg, J. L.; Dillavou, S.; Bonassar, L. J.; Cohen, I. Anatomic Variation of Depth-Dependent Mechanical Properties in Neonatal Bovine Articular Cartilage. *J. Orthop. Res.* **2013**, *31*, 686−691.
(50) Bartell, L. R.; Fortier, L. A.; Bonassar, L. J.; Cohen, I. Measuring Microscale Strain Fields in Articular Cartilage during Rapid Impact Reveals Thresholds for Chondrocyte Death and a Protective Role for the Superficial Layer. *J. Biomech.* **2015**, *48*, 3440−3446.
(51) Sevenler, D.; Buckley, M. R.; Kim, G.; van der Meulen, M. C. H.; Cohen, I.; Bonassar, L. J. Spatial Periodicity in Growth Plate Shear Mechanical Properties Is Disrupted by Vitamin D Deficiency. *J. Biomech.* **2013**, *46*, 1597−1603.
(52) Taylor, E. A.; Lloyd, A. A.; Salazar-Lara, C.; Donnelly, E. L. Raman and FT-IR Mineral to Matrix Ratios Correlate with Physical Chemical Properties of Model Compounds and Native Bone Tissue. *Appl. Spectrosc.* **2017**, *71*, 2404−2410.
(53) Mandair, G. S.; Morris, M. D. Contributions of Raman Spectroscopy to the Understanding of Bone Strength. *BoneKEy Rep.* **2015**, *4*, 1−8.
(54) Silverberg, J. L.; Barrett, A. R.; Das, M.; Petersen, P. B.; Bonassar, L. J.; Cohen, I. Structure-Function Relations and Rigidity Percolation in the Shear Properties of Articular Cartilage. *Biophys. J.* **2014**, *107*, 1721−1730.
(55) Blaber, J.; Adair, B.; Antoniou, A. Ncorr: Open-Source 2D Digital Image Correlation Matlab Software. *Exp. Mech.* **2015**, *55*, 1105−1122.
(56) Vedi, V.; Williams, A.; Tennant, S. J.; Spouse, E.; Hunt, D. M.; Gedroyc, W. M. W. Meniscal Movement an In-Vivo Study Using Dynamic Mri. *J. Bone Jt. Surg.* **1999**, *81B*, 37−41.
(57) Hauch, K. N.; Oyen, M. L.; Odegard, G. M.; Haut Donahue, T. L. Nanoindentation of the Insertional Zones of Human Meniscal Attachments into Underlying Bone. *J. Mech. Behav. Biomed. Mater.* **2009**, *2*, 339−347.
(58) Ferguson, V. L.; Bushby, A. J.; Boyde, A. Nanonmechanical Properties and Mineral Concentration in Articular Calcified Cartilage and Subchondral Bone. *J. Anat.* **2003**, *203*, 191−202.
(59) Mente, P. L.; Lewis, J. L. Elastic Modulus of Calcified Cartilage Is an Order of Magnitude Less than That of Subchondral Bone. *J. Orthop. Res.* **1994**, *12*, 637−647.
(60) Li, Y.; Asadi, A.; Monroe, M. R.; Douglas, E. P. PH Effects on Collagen Fibrillogenesis in Vitro: Electrostatic Interactions and Phosphate Binding. *Mater. Sci. Eng. C* **2009**, *29*, 1643−1649.
(61) Dong, M.; Xu, S.; Bünger, M. H.; Birkedal, H.; Besenbacher, F. Temporal Assembly of Collagen Type II Studied by Atomic Force Microscopy. *Adv. Eng. Mater.* **2007**, *9*, 1129−1133.
(62) Deymier, A. C.; Schwartz, A. G.; Cai, Z.; Daulton, T. L.; Pasteris, J. D.; Genin, G. M.; Thomopoulos, S. The Multiscale Structural and Mechanical Effects of Mouse Supraspinatus Muscle Unloading on the Mature Enthesis. *Acta Biomater.* **2019**, *83*, 302.
(63) Hu, Y.; Birman, V.; Deymier-Black, A. C.; Schwartz, A. G.; Thomopoulos, S.; Genin, G. M. Stochastic Interdigitation as a Toughening Mechanism at the Interface between Tendon and Bone. *Biophys. J.* **2015**, *108*, 431−437.
(64) Schwartz, A. G.; Long, F.; Thomopoulos, S. Enthesis Fibrocartilage Cells Originate from a Population of Hedgehog-Responsive Cells Modulated by the Loading Environment. *Development* **2015**, *142*, 196−206.
(65) Puetzer, J. L.; Koo, E.; Bonassar, L. J. Induction of Fiber Alignment and Mechanical Anisotropy in Tissue Engineered Menisci with Mechanical Anchoring. *J. Biomech.* **2015**, *48*, 1436−1443.
(66) McCorry, M. C.; Bonassar, L. J. Fiber Development and Matrix Production in Tissue-Engineered Menisci Using Bovine Mesenchymal Stem Cells and Fibrochondrocytes. *Connect. Tissue Res.* **2017**, *58*, 329−341.
(67) Ma, J.; Smietana, M. J.; Kostrominova, T. Y.; Wojtys, E. M.; Larkin, L. M.; Arruda, E. M. Three-Dimensional Engineered Bone−Ligament−Bone Constructs for Anterior Cruciate Ligament Replacement. *Tissue Eng., Part A* **2012**, *18*, 103−116.
(68) Priemel, T.; Degtyar, E.; Dean, M. N.; Harrington, M. J. Rapid Self-Assembly of Complex Biomolecular Architectures during Mussel Byssus Biofabrication. *Nat. Commun.* **2017**, *8*, No. 14539.
(69) Lee, B. P.; Messersmith, P. B.; Israelachvili, J. N.; Waite, J. H. Mussel Inspired Adhesives and Coatings. *Annu. Rev. Mater. Res.* **2011**, *41*, 99−132.
(70) Liu, L.; Jiang, Y.; Boyce, M.; Ortiz, C.; Baur, J.; Song, J.; Li, Y. The Effects of Morphological Irregularity on the Mechanical Behavior of Interdigitated Biological Sutures under Tension. *J. Biomech.* **2017**, *58*, 71−78.
(71) Hwang, B.-Y.; Kim, S.-J.; Lee, S.-W.; Lee, H.-E.; Lee, C.-K.; Hunter, D. J.; Jung, K.-A. Risk Factors for Medial Meniscus Posterior Root Tear. *Am. J. Sports Med.* **2012**, *40*, 1606−1610.
(72) Talari, A. C. S.; Zanyar, M.; Rehman, S.; Rehman, I. U. Raman Spectroscopy of Biological Tissues. *Appl. Spectrosc. Rev.* **2015**, *50*, 46−111.
(73) Kazanci, M.; Roschger, P.; Paschalis, E. P.; Klaushofer, K.; Fratzl, P. Bone Osteonal Tissues by Raman Spectral Mapping: Orientation-Composition. *J. Struct. Biol.* **2006**, *156*, 489−496.
(74) Schindelin, J.; Arganda-carreras, I.; Frise, E.; Kaynig, V.; Longair, M.; Pietzsch, T.; Preibisch, S.; Rueden, C.; Saalfeld, S.; Schmid, B.; et al. Fiji: An Open-Source Platform for Biological-Image Analysis. *Nat. Methods* **2012**, *9*, 676−682.
(75) Hovden, R.; Jiang, Y.; Xin, H. L.; Kourkoutis, L. F. Periodic Artifact Reduction in Fourier Transforms of Full Field Atomic Resolution Images. *Microsc. Microanal.* **2015**, *21*, 436−441.
(76) Junqueira, L. C. U.; Bignolas, G.; Brentani, R. R. Picrosirius Staining plus Polarization Microscopy, a Specific Method for Collagen Detection in Tissue Sections. *Histochem. J.* **1979**, *11*, 447−455.
(77) Dayan, D.; Hiss, Y.; Hirshberg, A.; Bubis, J. J.; Wolman, M. Are the Polarization Colors of Picrosirius Red-Stained Collagen Determined Only by the Diameter of the Fibers? *Histochemistry* **1989**, *93*, 27−29.

DOI: 10.1021/acsami.9b03595
ACS Appl. Mater. Interfaces 2019, 11, 26559−26570